A Least Squares Adjustment of Multi-temporal InSAR Data

Stéphane Le Mouélic, Daniel Raucoules, Claudie Carnec, Christine King

A Least Squares Adjustment of Multi-temporal InSAR Data: Application to the Ground Deformation of Paris

Stéphane Le Mouélic, Daniel Raucoules, Claudie Carnec, and Christine King

Abstract

Satellite radar interferometry can be used to spatially monitor small vertical ground deformations. When millimeter accuracy is required, the differential interferometry technique is hampered by the ambiguity with atmospheric artifacts. It is also often difficult to obtain a precise evaluation of the kinematic evolution of ground deformations from a set of time, randomly distributed interferograms. We present the results of a least-squares approach coupled with a temporal filtering and applied to a large data set over the City of Paris. The mean deformation rate and a map of areas affected by time, non-linear deformation events are presented. We show that this approach, which provides a chronologically ordered set of phase screens, allows the retrieval of the kinematic parameters of ground deformations as low as 1 to 2 mm per year. Subsiding areas have been detected, and their evolution in time has been quantified. Such an approach can be useful to fully characterize the kinematic evolution of ground deformations in major cities or desertic areas where large areas have a high degree of coherence and where millimeter accuracy is often required.

Introduction

Satellite radar interferometry has provided a new tool for monitoring slow-rate ground deformations in a wide range of geophysical applications (see Massonnet and Feigl, 1998 for a review). Ground motion hazards such as subsidence, uplift, landslides, or earthquakes can be monitored with an unsurpassed spatial coverage from remote sensing radar observations. The differential interferometry technique (D-InSAR) has been successfully applied to study ground deformations in major cities such as Napoli (Tesauro *et al.*, 2000), Mexico (Carnec *et al.*, 2000; Strozzi *et al.*, 2001), Bologna (Wegmüller *et al.*, 1999), Las Vegas (Amelung *et al.*, 1999; Hoffmann *et al.*, 2001) or Prato (Raucoules *et al.*, 2002). New insights are also revealed by the more advanced Permanent Scatterers Method (Ferretti *et al.*, 2000). Ancient quarries, mining activities, underground construction, water, or geothermal fluids extraction can result in subtle surface deformations. The information concerning the ground stability in densely urbanized areas is therefore a valuable tool for land use planning and natural or anthropogenic risk assessment.

When considering ground deformations as low as a few millimeters per year, a problem commonly faced with the D-InSAR technique is the ambiguity with atmospheric artifacts, which can be as high as one fringe (equivalent to 3 cm of vertical deformation) in single ERS interferograms. Another drawback is the restricted number of interferograms which can be derived from a set of images to characterize ground deformations. Indeed, only interferograms with sufficiently low perpendicular baseline values can be used to preserve the coherence level. This results most of the time in an uneven temporal distribution of the differential interferograms from which it is difficult to obtain a synoptic view of the kinematic parameters of ground deformations.

We present a modified version of a least squares inversion method first proposed by Usai *et al.* (1999, 2003) and also used by Lundgren *et al.* (2001) and which overcomes these limitations. The algorithm is applied to the City of Paris. The aim of this approach is to provide a chronologically ordered sequence of phase screens from a set of time, randomly-distributed interferograms. We will see that the least squares inversion method, coupled with a temporal filtering which uses the time uncorrelated nature of the atmospheric features, strongly improves the sensitivity of the D-InSAR technique and allows the monitoring of ground deformations as low as 1 to 2 mm per year. We also present the derivation of a mean deformation rate map and the automatic detection of areas affected by time, non-linear deformation events. The deformation history of each coherent pixel can be derived from this approach, similarly to what is obtained with the Permanent Scatterers Approach in large coherent areas (Ferretti *et al.*, 2000). We will see that this analysis confirms the conclusions obtained in a restricted area by Fruneau and Sarti (2000) and Le Mouelic *et al.* (2002) from classical differential interferometry, and allows the monitoring of much subtle ground deformations (up to 1 to 2 mm/year) than what was previously shown in these studies.

Description of the Data Set

The input data set consists of 30 ERS-1 and ERS-2 images covering the period 1992–2000. The characteristics of the data set are given in Table 1. The last column of this table

Stephane Le Mouélic is with the Laboratoire de Planétologie et Géodynamique, CNRS-Université de Nantes, 2 rue de la Houssinère BP 92208, 44322 Nantes cedex 3, France (stephane.lemouelic@chimie.univ-nantes.fr).

Daniel Raucoules, Claudie Carnec, Christine King are with the BRGM/ARN, 3 Avenue Claude GUILLEMIN, BP 6009, 45060 Orléans cedex 2, France.

Photogrammetric Engineering & Remote Sensing
Vol. 71, No. 2, February 2005, pp. 197–204.

0099-1112/05/7102–0197/$3.00/0

TABLE 1. CHARACTERISTICS OF THE ERS IMAGES USED IN THIS STUDY. THE LAST COLUMN DESCRIBES THE INTERFEROMETRIC COMBINATIONS WHICH WILL BE USED AS INPUT IN THE LEAST SQUARES INVERSION DISCUSSED IN A LATER SECTION. PERPENDICULAR BASELINES IN METERS AND TIME SPAN IN DAYS ARE RESPECTIVELY INDICATED IN BRACKETS FOR EACH PAIR

Orbit No.	Date	$B_\perp$(m)	Combined as First Image with Orbits Number:
4619	06/03/1992	48	15350 (48,2124), 19859 (103, 2439), 20494 (197, 1073), 21362 (41, 2544), 21496 (43, 1178), 28877(109, 3069), 3326 (53, 1284), 8837 (119,1669), 9839 (51, 1739)
5621	08/12/1992	−583	13847 (23, 1949), 22865 (110, 2579), 23366 (60, 2614), 16853 (53, 2159)
6122	09/16/1992	492	12344 (59, 1809), 22364 (88, 2509), 24001 (43, 1248), 26372 (36, 2789), 28376 (39, 2929)
20494	06/16/1995	−149	14348 (61, 946), 14849 (7, 981), 15350 (149, 1016), 19859 (84, 1331), 21362 (156, 1436), 8837 (78, 561)
21496	08/25/1995	5	never used first in an interferogram
3326	12/09/1995	101	15350 (101, 840), 19859 (167, 1155), 21362 (94, 1260), 25871 (122, 1575), 28877(56, 1785), 8837 (172, 385), 9839 (104, 465)
24001	02/16/1996	535	12344 (102, 561), 26372 (7, 1541), 28376 (4, 1681)
25504	05/31/1996	−336	14849 (180, 631), 17855(84, 841), 22865 (137, 1191)
7835	10/19/1996	551	26372 (23, 1295), 28376 (20, 1435)
8837	12/28/1996	−71	14348 (139, 385), 14849 (85, 420), 15350 (71, 455), 19859 (6, 875), 21362 (78, 875), 9839 (68, 70), 17354 (38, 595)
9839	03/08/1997	−21	14849 (153, 350), 15350 (21, 385), 17354 (106, 525), 19859 (44, 700), 21362 (10, 805), 28877 (160, 1330)
12344	08/30/1997	433	22364 (29, 700), 26372 (95, 980), 28376 (98, 1120), 29378 (51, 1190)
13346	11/08/1997	−333	17855 (87, 315), 22865 (140, 665)
13847	12/13/1997	−606	16853 (76, 210), 17855 (186, 280) , 22865 (133, 630), 23366 (37, 665)
14348	01/17/1998	−210	14849 (54, 35), 19859 (145, 385), 17354 (101, 210)
14849	02/21/1998	−156	15350 (156, 35), 19859 (91, 350), 21362 (163, 455), 17354 (47, 175)
15350	03/28/1998	0	19859 (65, 315), 21362 (7, 420), 28877 (157, 945), 17354 (109, 140)
16853	07/11/1998	−530	17855 (110, 70), 22865 (57, 420), 23366 (113, 455)
17354	08/15/1998	−109	19859 (44, 175), 21362 (116, 280)
17855	09/19/1998	−420	22865 (53, 350)
19859	02/06/1999	−65	21362 (74, 105)
21362	05/22/1999	9	28877 (150, 525)
22364	07/31/1999	404	never used first
22865	09/04/1999	−473	23366 (170, 35)
23366	10/09/1999	−643	never used first
25871	04/01/2000	223	28877 (66, 210), 29378 (159, 245)
26372	05/06/2000	528	28376 (3, 140) , 29378 (146, 210)
28376	09/23/2000	531	29378 (149, 70)
28877	10/28/2000	157	never used first
29378	12/02/2000	382	never used first

describes the relevant interferometric combinations which will be used later in this study. Figure 1 shows the mean radar amplitude image of the test site. This area is densely urbanized, and it therefore provides a high degree of coherence due to the geometric and radiometric stability of the constructions.

Data Processing Steps for the Least Squares Inversion Method

Image Coregistration and Computation of the Interferograms

ERS Single Look Complex images are first co-registered at a sub-pixel level to a master reference image. The reference image should preferably be an image having a median perpendicular baseline value with respect to the set of images so as to minimize distortions errors which could hamper the co-registration process. The image number "15350" was consequently taken as reference. This process raised the question of a possible loss of coherence due to errors in the co-registration with the master image of both images of the interferometric pair. This question was taken into consideration by testing the least favorable case (image 4118, 29 April 1992, $B_\perp = -1037$ m; and image 4829, 23 March 1996, $B_\perp = -1061$ m with respect to the 15350 master image). No significant loss of coherence was observed for this interferometric pair. It therefore legitimizes the use of a single reference image for the co-registration of the whole set of images.

We have automatically produced the entire set of 241 interferometric combinations which have perpendicular baseline ($B_\perp$) values shorter than 200 m. This baseline limit is chosen to avoid geometric decorrelation and minimize residual topographic artifacts. Orbital fringes are removed automatically by finding their frequency using a Fast Fourier Transform (FFT) computation. This technique gives accurate results in flat areas such as the Paris site. The topographic component of the phase has been removed using a Digital Elevation Model (DEM) provided by the French National Geographic Institute (IGN) with a 50 m resolution and a $dh = 2.5$ m vertical accuracy. Interferograms have been geocoded with a 25 m pixel size. An adaptive filter (Goldstein and Werner, 1998) has been applied to improve the signal to noise ratio of the interferograms.

The phase error induced by DEM inaccuracy is equal to $2\pi\ dh\ Bp/10000$, where Bp is the perpendicular baseline. The highest perpendicular baseline which has been used in our study is 197 m, corresponding to a topography phase error of less than a twentieth of a fringe. Possible errors introduced by the DEM are therefore negligible.

Unwrapping and Normalizing the Interferograms

Among the 241 combinations which have been produced, we have kept $M = 87$ interferograms whose coherence level is high enough (>0.4) on the area to be studied. These 87 interferometric pairs are given in the last column of Table 1. We have automatically unwrapped these interferograms using the minimum cost flow (Costantini, 1998) and Delaunay triangulation method (Marshall and Eppstein, 1992; Rosen and Costantini, 1999) implemented in the GAMMA software (Werner *et al.*, 2002). Each unwrapped

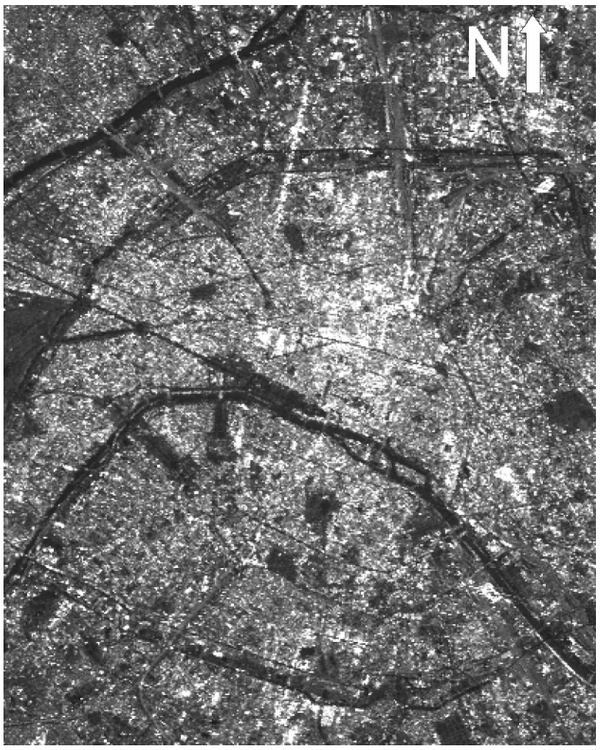

Figure 1. Mean amplitude image of the study area (the City of Paris, France).

interferogram has been multiplied by the factor $\lambda/4\pi \cos i$ (where $\lambda = 5.6$ cm is the radar wavelength and $i = 23°$ the incidence angle) to convert the phase values into equivalent vertical deformation values in centimeters.

The resulting unwrapped phase values are randomly shifted by an unknown, pixel-independent, constant value due to the 2π radians phase ambiguity, therefore, the unwrapped interferograms have to be normalized. Lundgren *et al.* (2001) selected a fixed point far from the subsidence pattern in their study area and forced the corresponding phase values to zero. Instead of selecting an arbitrary fixed point, we decided to correct each unwrapped interferogram by using a second-order polynomial fit to the data. This polynomial fit accounts for the unknown constant value and has a lower sensitivity to small-scale atmospheric artifacts which could affect any point chosen as a reference. It also corrects any residual linked to orbital fringes. It should be noted that this fit could also eliminate a parabolic ground deformation affecting the whole area (such as the one studied in Carnec *et al.*, 2000). A simple visual analysis of single interferograms is used to evaluate the possibility of such a deformation to occur which was not the case in our study.

Computation of the Mean Deformation Rate

At this stage, each unwrapped interferogram, once normalized by the method described above, can be translated in ground deformation rate by taking into account its time span. This can be used to compute a mean deformation rate map. The case of time, non-linear events will be discussed in a later stage. A simple arithmetic averaging of deformation screens normalized by their time span would give a higher weight to the pairs having the shortest time spans. These pairs have also the lowest signal (deformation) to noise (mainly atmospheric artifacts) ratio. We therefore used a weighted averaging method which optimizes the contribution of interferograms in terms of signal to noise ratio. In this approach, the estimated mean deformation rate is obtained by a least squares optimization. Assuming that the temporal evolution of the deformations is a constant v, the estimated value $\hat{v}$ is given by, $\Delta\mathbf{h} = \hat{v}\Delta\mathbf{t}$, where $\Delta\mathbf{h}$ and $\Delta\mathbf{t}$ are vectors of M rows containing respectively the unwrapped phase values converted into vertical deformation in centimeter and the interferogram time spans. $\hat{v}$ is therefore given by:

$$\hat{v} = \Delta\mathbf{t}^t\Delta\mathbf{h} \times (\Delta\mathbf{t}^t\Delta\mathbf{t})^{-1} = \frac{\sum_{i=0}^{M-1} \Delta t_i \times \Delta h_i}{\sum_{i=0}^{M-1} \Delta t_i^2} \quad (1)$$

where $M = 87$ is the number of interferograms used, Δt_i is the time span of interferogram i and Δh_i, its unwrapped phase value converted into vertical deformation in centimeter. The combination of the whole set of interferograms in a mean deformation rate allows the elimination of residual atmospheric features (Figure 2). We see that deformation patterns as small as 1 to 2 mm per year can easily be distinguished (arrow "a" corresponding to the "Grand Palais" area, and arrow "c" corresponding to the "Montmartre" area). These deformation patterns, whose kinematic evolution will be discussed later, had never been observed previously from

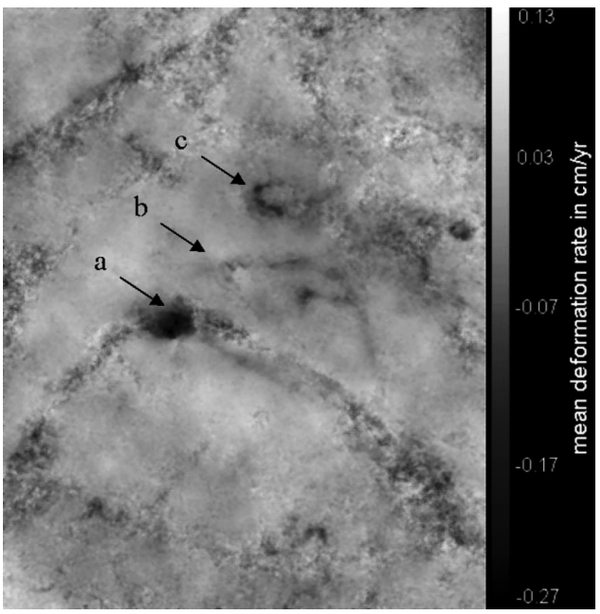

Figure 2. Mean deformation rate $\hat{V}$ computed from Equation 1 on the set of 87 interferograms and displayed in gray levels from −0.3 cm/yr (black) to 0.2 cm/yr (white). Arrow "a" indicates a mean subsidence event of −3 mm/yr in the Grand Palais area during the period 1992–2000. Arrow "b" corresponds to the Saint-Lazare area studied in Fruneau and Sarti (2000) and Le Mouelic *et al.* (2002). Up and down deformations tends to compensate during the 1992–2000 period in this area. Arrow "c" corresponds to a subsidence of −2 mm/yr around the Montmartre area. The temporal profiles of these areas will be shown in Figure 3.

remote sensing data. The subsidence event in the Grand Palais area is confirmed by ground truth studies which will be explained in the discussion section.

An important issue is the quantification of the residual atmospheric noise level in the mean deformation map produced from Equation 1. Indeed, some images appear several times in the selected interferometric combinations used as input. For example, the scene 4619 is used in eight interferograms, whereas the scene 7835 is used only in two interferograms. This raised the question of a possible over-representation of the atmospheric phase contribution of such multiple scenes. It should first be noted that the most-used image appears only eight times on a total of 87 input interferograms. This indicates qualitatively that an averaging effect is obtained. In order to quantify this averaging effect, we have performed several simulations using a random value for the atmospheric components of each phase screen on a pixel-by-pixel basis. For this test, the deformation component is supposed to be zero and the atmospheric component (therefore corresponding to Δh_i in Equation 1) is a random Gaussian value centered on zero and with a 1-sigma width of 3 cm. This corresponds to a rather high value for atmospheric artifacts according to Williams *et al.* (1998). A set of 200 independent draws have been performed using Equation 1. The standard deviation value of these 200 draws gives an estimation of a residual atmospheric component which is equivalent to less than 0.5 mm per year. This is well below the 1 to 2 mm per year deformation features that where highlighted in Figure 2.

The mean deformation rate given by Equation 1 is a powerful tool for quantifying time linear deformations. On the other hand, a time, non-linear deformation such as the one observed by Fruneau and Sarti (2000) and Le Mouélic *et al.* (2002) in the south of the Saint-Lazare area (downwards, and then upwards, deformations) tends to compensate on this image (arrow "b" in Figure 2). The least squares inversion and temporal filtering, which will now be explained, will permit a deeper analysis of the kinematic evolution of these areas during the period 1992 to 2000.

Least Squares Inversion: Computation of a Deformation Screen for Each Date

The next step of the process is the least squares inversion of the system of normalized unwrapped interferograms. The procedure is described in details in Usai *et al.* (1999) and in Lundgren *et al.* (2001). It corresponds to the inversion, on a pixel by pixel basis, of the system $\mathbf{Y} = \mathbf{AX}$ where $\mathbf{Y}$ is a vector containing the set of $M = 87$ unwrapped interferograms, A is a N $\times$ M matrix filled with values of 0, 1 and -1 and X a vector containing the set of phases of the $N = 30$ dates (the chronologically ordered phase screens). For the input interferogram number k (corresponding to the difference of two phase screens at dates i and j), the values of $\mathbf{A}$ on row k are all zero except at columns i and j, where they are $+1$ and -1. The solution of this linear system is given by the matrix equation:

$$\mathbf{X} = (\mathbf{A}^t\mathbf{A})^{-1}\mathbf{A}^t\mathbf{Y} \tag{2}$$

where the first date in $\mathbf{X}$ (taken as the reference phase screen) and the first column of $\mathbf{A}$ have not been considered. The inversion is possible only if the determinant of the matrix $\mathbf{A}^t\mathbf{A}$ is different from zero. A determinant equals to zero would indicate that clusters of interferograms in the input data set are disconnected (no common date). This is due to the fact that some dates appear only once, often because low baseline values, which are needed to preserve the coherence level, are not always available. In this case, the link between clusters of interferograms can be artificially reintroduced by generating flat or interpolated interferograms on periods as short as possible (Usai *et al.*, 1999). In our case, the whole set of interferograms was connected. The result of the inversion is a set of $N - 1 = 29$ chronologically ordered phase screens from which the automatic detection of non-linear deformation events can be performed.

Automatic Detection of Non-Linear Deformations

The automatic discrimination between atmospheric features and time, non-linear events is a problem of importance. Nevertheless, it is possible to derive automatically the areas affected by time, non-uniform deformations by using the elements described previously. Indeed, the mean deformation rate computed from Equation 1 (and shown in Figure 2) can be used to evaluate the amount of expected linear deformation for each date. When this contribution is subtracted from a phase screen (the output of the least square inversion), two contributions remain: the atmospheric contribution of the given date, and the deviations from the linear deformation model. Atmospheric features are totally independent from one phase screen to the next, whereas ground deformations are spatially at the same location. The quadratic mean of the phase screens, from which the linear deformation model (evaluated by Equation 1) has been previously subtracted, therefore allows for the detection of the areas affected by time, non-uniform deformation events. This is shown in Figure 3 which displays the result of Equation 3:

$$\sigma_{NL} = \sqrt{\frac{1}{N}\sum_{i=0}^{N-1}(d_i - \hat{v} \times \Delta t_i)^2} \tag{3}$$

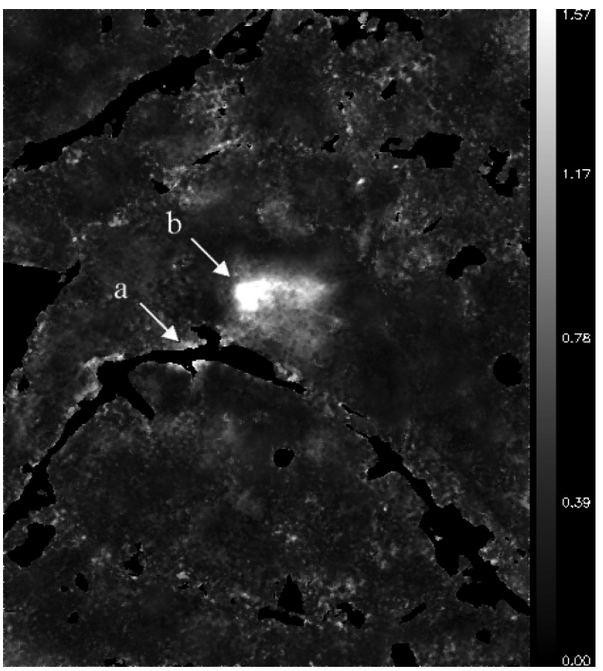

Figure 3. Standard deviation (in cm) from the linear deformation model obtained by applying Equation 3. This image emphasizes areas affected by time, non-linear ground deformation (in white). As expected, the Saint-Lazare area (arrow "b") appears clearly in the center of this image. Areas having a mean coherence value lower than 0.7 have been set to zero in order to facilitate the interpretation.

where σ_{NL} represents the standard deviation from a linear deformation model, N is the number of dates, d_i corresponds to the deformation value of the i^{th} phase screen, $\hat{v}$ is the mean deformation rate computed from Equation 1 and Δt_i is the time interval between the date i and the reference date.

Figure 3 clearly indicates that the area south of the Saint-Lazare railway station (arrow "b") and also to a lesser extent the Grand Palais area (arrow "a") are affected by time, non-linear deformations on the period studied. This is consistent with the conclusions made by Fruneau and Sarti (2000) and Le Mouélic *et al.* (2002) from classical interferometry for the Saint-Lazare area. If the quantitative signification of the result given by Equation 2 is not obvious, the qualitative information provided on the nature of the deformations is relevant for the following discussion. The temporal deformation profiles, which will now be discussed, will allow the quantification of the non-linear behavior.

Application of a Temporal Filtering and Derivation of Temporal Series

The deformations monitored by Lundgren *et al.* (2001) on the Campi Flegrei caldera with the least squares inversion method have an amplitude of approximately 20 cm. Therefore, atmospheric features, which have a typical amplitude of one-third of a fringe (corresponding to a vertical deformation of 1 cm) in a single interferogram (Williams *et al.*, 1998; Goldstein, 1995), do not hamper the interpretation of the deformation patterns in their chronologically-ordered sequence of phase screens. In our case, the maximum amplitude of the deformation patterns is lower than 2 cm (in the south of the Saint-Lazare area), and the continuous movements which we want to emphasize are as low as few millimeters per year. Therefore, the atmospheric components of the chronologically-ordered phase screens of Paris limits the conclusion which can be made from the direct output of the least squares inversion method.

We have used the physical property of the atmospheric component to bypass this problem. Indeed, excepted for areas with very steep relief (Delacourt, 1998), atmospheric features are totally uncorrelated in time, and are therefore, completely different from one date to the next. On the contrary, ground deformation signatures are correlated in time. Therefore, using a temporal filter on a pixel-by-pixel basis reduces the atmospheric noise without degrading the information regarding slow rate ground deformations. We have used a Lee filter (Lee, 1980) in the temporal dimension to improve the reduction of the residual atmospheric artifacts in the chronologically-ordered sequence of phase screens. The Lee filter smoothes additive image noise by generating statistics in a local neighborhood and comparing them to the expected values. Figure 4 displays the result for three temporal profiles of the deformations occurring in the Grand Palais area (Figure 4a), south of the Saint-Lazare railway station (Figure 4b: time, non-linear evolution) and Montmartre area (Figure 4c: time linear).

Plus symbols in Figure 4 correspond to the direct output of the least squares inversion method. Asterisks correspond to the values filtered using the Lee filter with a window of 5 pixels (in time) to reduce the atmospheric component. This width of 5 pixels in low enough to preserve seasonal variations if any are present. Figures 4a and 4c show that a significant improvement is obtained for time regular ground deformations. In the case of strong time, non-linear deformations, and in particular in the case of a significant ground deformation occurring in less than the 35 days time sample frequency, the temporal filter would tend to widen the time interval during which the deformation occurs. We have used Figure 3 to detect such time, non-linear events, and a visual

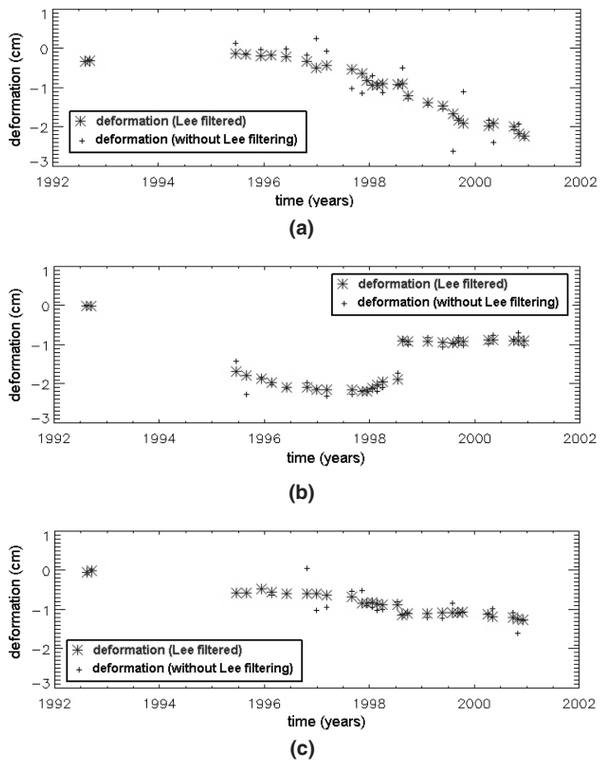

Figure 4. Temporal deformation profiles obtained after the least squares inversion and temporal filtering: (a) Grand Palais subsiding area. (b) Saint-Lazare-Condorcet area. (c) Montmartre area. These areas correspond to the arrows in Figure 2. The temporal filtering allows a significant reduction of the atmospheric contribution.

analysis of the unfiltered chronologically-ordered sequence of phase screens to derive the exact dates of the discontinuities. The strongest discontinuity (uplift) was found in the Saint-Lazare area during the summer 1998. This uplift also appears in the unfiltered deformation profile of Figure 4b. The Lee temporal filtering in Figure 4b has been applied separately in two parts (16 June 1995 to 11 July 1998, and 15 August 1998 to 2 December 2000) to preserve this discontinuity.

Plate 1 shows a set of representative deformation phase screens (in chronological order) which have been produced by the least squares inversion and the temporal Lee filtering. Such a sequence could be used to produce an animated sequence showing the evolution of the deformation. One cycle of color represents a vertical deformation of 1.5 cm in these images. This sequence clearly shows the time evolution of the deformation in the south of the St-Lazare area (subsidence, and then uplift). The small residual subsidence feature still observed south of the Saint Lazare railway station in the last phase screen seems to indicate that the uplift observed by Le Mouelic *et al.* (2002) do not fully compensate the subsidence observed by Fruneau and Sarti (2000). This question was left unanswered at the time of these studies. The sequence also reveals the millimetric deformations in the Grand Palais and Montmartre areas which mostly appear in the last phase screens due to their low deformation rate.

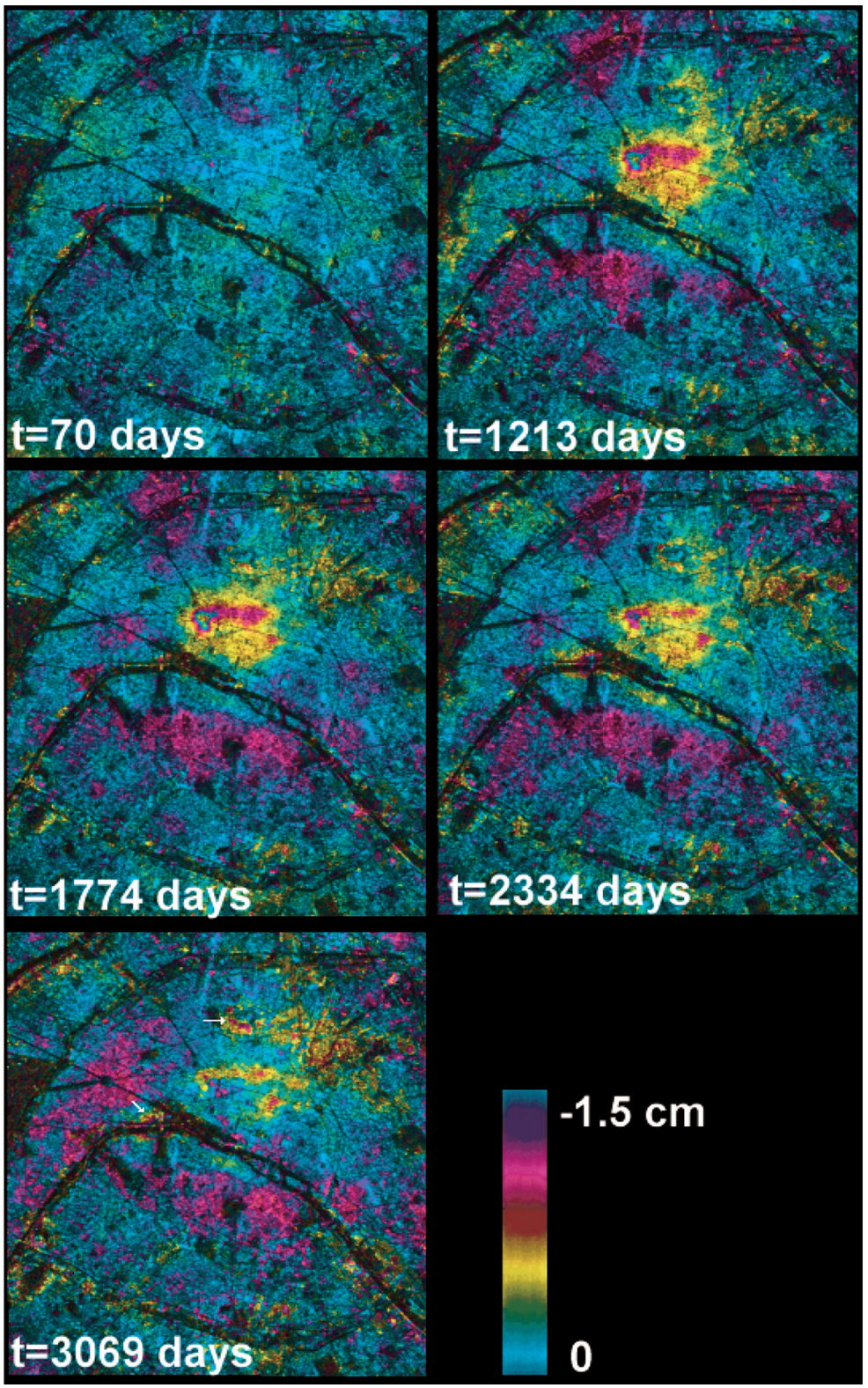

Plate 1. Set of representative phase screens (with respect to the 03 June 1992) obtained after the least squares inversion and the temporal Lee filtering performed on five dates. One cycle of color represents a deformation of 1.5 cm in these images. The mean amplitude image has been used as background.

Discussion

Effect of a Weighting by the Coherence Level in the Least Squares Computation

Some interferograms have a lower degree of coherence than others, due to large perpendicular baseline values and/or surface changes (humidity or vegetation changes). Figure 5 shows the mean coherence on the area which has been computed by averaging the set of 87 individual coherence images. The mean coherence is displayed in gray levels between 0 (black) and 1 (white). As expected, water and vegetated areas appear as low values in this image, whereas urbanized areas appear in high values.

We have tested the coherence level as a weighting factor for each interferogram in the least-squares inversion process. This test showed that in the case of Paris, the improvement is not significant enough (lower than 2 mm) to allow a better interpretation of the temporal profiles.

Standard Deviation of the Results

As a result of the least squares inversion, the standard deviation of each pixel with respect to the input data set is also obtained. In order to evaluate the link between this standard deviation and the coherence level, we have compared the spatial variations of the standard deviation of each phase screen with the expected standard deviation due to a coherence loss which is approximated by the Cramer-Rao bound (Zebker and Villasenor, 1992) given by:

$$\sigma_\Phi = \frac{1}{\sqrt{2N_L}} \frac{\sqrt{1-\rho^2}}{\rho} \tag{4}$$

where N_L corresponds to the number of looks and ρ to the coherence level. In our case, the mean coherence was estimated using 5×5 pixels windows on interferograms previously filtered by an adaptive filter (Goldstein and Werner, 1998). The actual value of N_L is therefore not known, but it is the same for each pixel in all phase screens. Figure 6 shows that the standard deviation after the least squares inversion is linearly correlated to the standard deviation inferred from the mean coherence level. This confirms that the mean coherence level is the driving factor controlling the accuracy of the result.

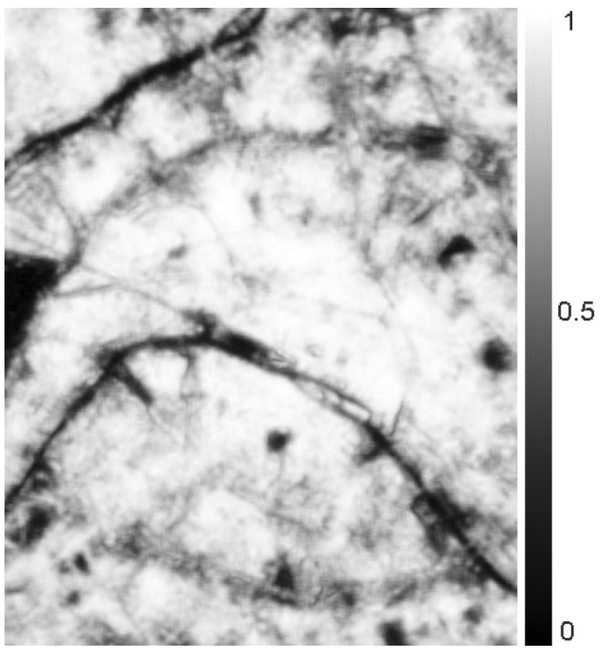

Figure 5. Mean coherence image of the set of 87 interferograms used in this study displayed in gray levels between 0 (black) and 1 (white).

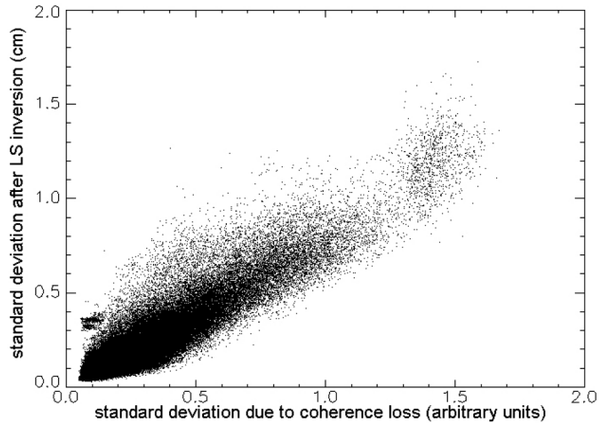

Figure 6. Comparison of the standard deviation of the first phase screen obtained by the least square inversion with the standard deviation estimated from the mean coherence using the Cramer-Rao bound (Equation 4). The correlation between the two parameters shows that the accuracy of the result of the least square inversion is mainly controlled by the coherence level.

Origin of the Observed Deformations

The Saint-Lazare-Condorcet area corresponds to the location of an important underground construction site. This underground work was required to lower temporally the piezometric level by intensively pumping the underground water. The variations of the underground water level are most probable at the origin of the observed deformation in this area.

The Grand Palais and Montmartre deformations had never been observed before at this global scale and during this period. The Grand Palais is a major element of Paris heritage. It has been affected by subsidence since its construction between 1897 and 1900 for the World Fair. The present geological context results from the presence of an old river arm which induces poor soil conditions in the southern part of the site (containing silts, loose sands, and weathered limestone) compared to the northern part (made of dense fine to coarse sands and slightly weathered limestone). In addition, the masonry structures of the Grand Palais are supported by driven wooden piles on the southern part, whereas the columns are supported by spread masonry footings in the northern part. Driven wooden piles were rotten due to their exposure to oxidizing free air during a lowering of the water table. As a result, structural disorders and differential settlements have occurred since 1910. The total settlements are estimated to be around 10 to 15 centimeters, and up to 5 cm between 1972 and 2001. A global remedial works has been started at the end of 2001 to consolidate the foundation and the structure of the building. Our study shows that the Grand Palais is located in a globally unstable area for which relative stability was observed during

1992–1996, whereas about 2.5 cm of subsidence occurred between 1996 and the end of year 2000. Such information contributes to the overall comprehension of the phenomenon and could be integrated in a global monitoring strategy for the conservation of the building. We plan in future works to perform a more detailed comparison with other InSAR and geodetic data covering this area.

Conclusion

A least squares approach coupled with a temporal filtering has been used for monitoring small ground deformations from a set of 30 ERS images of the City of Paris. A method for computing the mean deformation rate and a map of areas affected by time, non-linear deformation events has also been presented. The aim of this approach is to provide a chronologically-ordered sequence of phase screens showing the kinematic evolution of the deformation patterns. The advantage of this method compared to the analysis of single interferograms is to allow a subsequent reduction of the atmospheric artifacts by using temporal filtering. Deformation features as low as 1 to 2 mm per year can easily be identified with this method. Subsiding areas have been detected in the Grand Palais and Montmartre areas. As a result, a synoptic view of Paris main ground deformations in the period 1992–2000 has been obtained. Such an approach provides important information concerning land use planning and natural (or anthropogenic) risk assessment in densely urbanized areas. This approach could also be useful to detect and quantify deformations associated with slow active faults in semi-desert areas when a millimetric accuracy is required.

Acknowledgments

This work was conducted in the framework of the RESUM project supported by CNES, the RTE and RGCU French technological networks, and the BRGM research direction. Authors are very grateful to two anonymous reviewers for their constructive comments. ERS images were provided by CNES.

References

Amelung, F., D. Galloway, J. Bell, H. Zebker, and R. Laczniak, 1999. Sensing the ups and downs of Las Vegas: InSAR reveals structural control of land subsidence and aquifer-system deformation, *Geology*, 27:483–486.

Carnec, C., A. Huré, E. Ledoux, D. Raucoules, A. Rivera, 2000. Mapping and modeling of major urban subsidence on Mexico City from radar interferometry, *International Conference: The Fragile Territory, Research and Application on Hydrogeological Disarray in the World*, 07–10 December, Rome, Italy.

Costantini, M., 1998. A novel phase unwrapping method based on network programming, *IEEE Transactions on Geoscience and Remote Sensing*, 36:813–821.

Delacourt, C., P. Briole, and J. Achache, 1998. Tropospheric corrections of SAR interferograms with strong topography: Application to Etna, *Geophysical Research Letters*, 25:2849–2853.

Ferretti, A., C. Pratti, and F. Rocca, 2000. Nonlinear subsidence rate estimation using permanent scatterers in differential SAR interferometry, *IEEE Transactions on Geoscience and Remote Sensing*, 38:2202–2212.

Fruneau, B. and F. Sarti, 2000. Detection of Ground Subsidence on the city of Paris using Radar Interferometry: isolation, of deformation from atmospheric artifacts using correlation, *Geophysical Research Letters*, 28:3981–3984.

Goldstein, R., 1995. Atmospheric limitations to repeat-track radar interferometry, *Geophysical Research Letters*, 22:2517–2520.

Goldstein, R., C. Werner, 1998. Radar interferogram filtering for geophysical applications, *Geophysical Research Letters*, 21:4035–4038.

Hoffmann, J., H.A. Zebker, D.L. Galloway, and F. Amelung, 2001. Seasonal subsidence and rebound in Las Vegas Valley, Nevada, observed by synthetic aperture radar interferometry, *Water Resources Research*, 37:1551–1566.

Lee, J.S., 1980. Digital image enhancement and noise filtering by use of local statistics, *IEEE Transactions on Pattern Analysis and Machine Intelligence*, 2:165–168.

Le Mouélic, S., D. Raucoules, C. Carnec, C. King, and F. Adragna, 2002. A ground uplift in the city of Paris (France) detected by satellite radar interferometry, *Geophysical Research Letters*, 29:1853–1856.

Lundgren, P., S. Usai, E. Sansosti, R. Lanari, M. Tesauro, G. Fornaro, and P. Berardino, 2001. Modeling surface deformation observed with synthetic aperture radar interferometry at Campi Flegrei caldera, *Journal of Geophysical Research*, 106:19355–19366.

Marshall, B., and D. Eppstein, 1990. *Mesh Generation and optimal triangulation, Computing in Euclidian Geometry* (Dhing-Zhu Du and Frank Hwang, editors), World Scientific, Singapore, pp. 23–90.

Massonnet, D., and K.L. Feigl, 1998. Radar interferometry and its application to changes in the Earth's surface, *Reiew of Geophysics*, 4:441–494.

Raucoules, D., S. Le Mouélic, C. Carnec, C. Maisons, and C. King, 2002. Urban subsidence in the city of Prato (Italy) monitored by satellite radar interferometry, *International Journal of Remote Sensing*, 24(4):891–897.

Rosen, P.A., and M. Costantini, 1999. A generalized phase unwrapping approach for sparse data, *Proceedings of IGARSS*, 28 June-2 July, Hambourg, Germany, unpaginated CDROM.

Strozzi, T., U. Wegmüller, L. Tosi, G. Bitelli, and V. Spreckels, 2001. Land subsidence monitoring with differential SAR interferometry, *Photogrammetric Engineering & Remote Sensing*, 67:1261–1270.

Tesauro, M., P. Berardino, R. Lanari, E. Sansisti, G. Fornaro, and G. Franschetti, 2000. Urban subsidence inside the city of Napoli (Italy) observed by satellite radar interferometry, *Geophysical Research Letters*, 27:1961–1964.

Usai, S., C. Delgaudio, S. Borgstrom, and V. Achilli, 1999. Monitoring terrain deformations at Phlegrean Fields with SAR interferometry, *2nd International Workshop on SAR Interferometry (FRINGE99),* European Space Agency, Liege, Belgium, unpaginated CDROM.

Usai, S., 2003. A Least Squares Database Approach for SAR interferometric data, Monitoring terrain deformations at Phlegrean Fields with SAR interferometry, *IEEE Transactions on Geoscience and Remote Sensing*, 41:753–760.

Werner, C., U. Wegmüller, and T. Strozzi, 2002. Processing strategies for phase unwrapping for InSAR applications, *Proceedings of EUSAR Conference*, 04–06 June, Cologne, Germany, unpaginated CDROM.

Williams, S., Y. Bock, and P. Fang, 1998. Integrated satellite interferometry: tropospheric noise, GPS estimates and implications for interferometric synthetic aperture products, *Journal of Geophysical Research*, 11:27051–27067.

Wegmüller, U., T. Strozzi, and G. Bitelli, 1999. Validation of ERS differential SAR interferometry for land subsidence mapping: the Bologna case study, *Proceedings of IGARSS'99*, 28 June-02 July, Hambourg, Germany, unpaginated CDROM.

Zebker, H.A., and J. Villasenor, 1992. Decorrelation in interferometric radar echoes, *IEEE Transactions on Geoscience and Remote Sensing*, 5:950–959.

(Received 24 June 2003; accepted 22 August 2003; revised 12 September 2003)